The Astrophysical Journal, 910:4 (14pp), 2021 March 20 https://doi.org/10.3847/1538-4357/abe123

Follow-up of Astrophysical Transients in Real Time with the IceCube Neutrino Observatory

R. Abbasi[1], M. Ackermann[2], J. Adams[3], J. A. Aguilar[4], M. Ahlers[5], M. Ahrens[6], C. Alispach[7], A. A. Alves, Jr.[8], N. M. Amin[9], R. An[10], K. Andeen[11], T. Anderson[12], I. Ansseau[4], G. Anton[13], C. Argüelles[10], S. Axani[14], X. Bai[15], A. Balagopal V.[16], A. Barbano[7], S. W. Barwick[17], B. Bastian[2], V. Basu[16], V. Baum[18], S. Baur[4], R. Bay[19], J. J. Beatty[20,21], K.-H. Becker[22], J. Becker Tjus[23], C. Bellenghi[24], S. BenZvi[25], D. Berley[26], E. Bernardini[2,58], D. Z. Besson[27,59], G. Binder[19,28], D. Bindig[22], E. Blaufuss[26], S. Blot[2], S. Böser[18], O. Botner[29], J. Böttcher[30], E. Bourbeau[5], J. Bourbeau[16], F. Bradascio[2], J. Braun[16], S. Bron[7], J. Brostean-Kaiser[2], A. Burgman[29], R. S. Busse[31], M. A. Campana[32], C. Chen[33], D. Chirkin[16], S. Choi[34], B. A. Clark[35], K. Clark[36], L. Classen[31], A. Coleman[9], G. H. Collin[14], J. M. Conrad[14], P. Coppin[37], P. Correa[37], D. F. Cowen[12,38], R. Cross[25], P. Dave[33], C. De Clercq[37], J. J. DeLaunay[12], H. Dembinski[9], K. Deoskar[6], S. De Ridder[39], A. Desai[16], P. Desiati[16], K. D. de Vries[37], G. de Wasseige[37], M. de With[40], T. DeYoung[35], S. Dharani[30], A. Diaz[14], J. C. Díaz-Vélez[16], H. Dujmovic[8], M. Dunkman[12], M. A. DuVernois[16], E. Dvorak[15], T. Ehrhardt[18], P. Eller[24], R. Engel[8], J. Evans[26], P. A. Evenson[9], S. Fahey[16], A. R. Fazely[41], S. Fiedlschuster[13], A. T. Fienberg[12], K. Filimonov[19], C. Finley[6], L. Fischer[2], D. Fox[38], A. Franckowiak[2,23], E. Friedman[26], A. Fritz[18], P. Fürst[30], T. K. Gaisser[9], J. Gallagher[42], E. Ganster[30], S. Garrappa[2], L. Gerhardt[28], A. Ghadimi[43], C. Glaser[29], T. Glauch[24], T. Glüsenkamp[13], A. Goldschmidt[28], J. G. Gonzalez[9], S. Goswami[43], D. Grant[35], T. Grégoire[12], Z. Griffith[16], S. Griswold[25], M. Gündüz[23], C. Haack[24], A. Hallgren[29], R. Halliday[35], L. Halve[30], F. Halzen[16], M. Ha Minh[24], K. Hanson[16], J. Hardin[16], A. A. Harnisch[35], A. Haungs[8], S. Hauser[30], D. Hebecker[40], K. Helbing[22], F. Henningsen[24], E. C. Hettinger[35], S. Hickford[22], J. Hignight[44], C. Hill[45], G. C. Hill[46], K. D. Hoffman[26], R. Hoffmann[22], T. Hoinka[47], B. Hokanson-Fasig[16], K. Hoshina[16,60], F. Huang[12], M. Huber[24], T. Huber[8], K. Hultqvist[6], M. Hünnefeld[47], R. Hussain[16], S. In[34], N. Iovine[4], A. Ishihara[45], M. Jansson[6], G. S. Japaridze[48], M. Jeong[34], B. J. P. Jones[49], R. Joppe[30], D. Kang[8], W. Kang[34], X. Kang[32], A. Kappes[31], D. Kappesser[18], T. Karg[2], M. Karl[24], A. Karle[16], U. Katz[13], M. Kauer[16], M. Kellermann[30], J. L. Kelley[16], A. Kheirandish[12], J. Kim[34], K. Kin[45], T. Kintscher[2], J. Kiryluk[50], S. R. Klein[19,28], R. Koirala[9], H. Kolanoski[40], L. Köpke[18], C. Kopper[35], S. Kopper[43], D. J. Koskinen[5], P. Koundal[8], M. Kovacevich[32], M. Kowalski[2,40], K. Krings[24], G. Krückl[18], N. Kurahashi[32], A. Kyriacou[46], C. Lagunas Gualda[2], J. L. Lanfranchi[12], M. J. Larson[26], F. Lauber[22], J. P. Lazar[10,16], K. Leonard[16], A. Leszczyńska[8], Y. Li[12], Q. R. Liu[16], E. Lohfink[18], C. J. Lozano Mariscal[31], L. Lu[45], F. Lucarelli[7], A. Ludwig[35,51], W. Luszczak[16], Y. Lyu[19,28], W. Y. Ma[2], J. Madsen[16], K. B. M. Mahn[35], Y. Makino[16], P. Mallik[30], S. Mancina[16], I. C. Mariş[4], R. Maruyama[52], K. Mase[45], F. McNally[53], K. Meagher[16], A. Medina[21], M. Meier[45], S. Meighen-Berger[24], J. Merz[30], J. Micallef[35], D. Mockler[4], G. Momenté[18], T. Montaruli[7], R. W. Moore[44], R. Morse[16], M. Moulai[14], R. Naab[2], R. Nagai[45], U. Naumann[22], J. Necker[2], L. V. Nguyễn[35], H. Niederhausen[24], M. U. Nisa[35], S. C. Nowicki[35], D. R. Nygren[28], A. Obertacke Pollmann[22], M. Oehler[8], A. Olivas[26], E. O'Sullivan[29], H. Pandya[9], D. V. Pankova[12], N. Park[16], G. K. Parker[49], E. N. Paudel[9], P. Peiffer[18], C. Pérez de los Heros[29], S. Philippen[30], D. Pieloth[47], S. Pieper[22], A. Pizzuto[16], M. Plum[11], Y. Popovych[30], A. Porcelli[39], M. Prado Rodriguez[16], P. B. Price[19], B. Pries[35], G. T. Przybylski[28], C. Raab[4], A. Raissi[3], M. Rameez[5], K. Rawlins[54], I. C. Rea[24], A. Rehman[9], R. Reimann[30], M. Renschler[8], G. Renzi[4], E. Resconi[24], S. Reusch[2], W. Rhode[47], M. Richman[32], B. Riedel[16], S. Robertson[19,28], G. Roellinghoff[34], M. Rongen[30], C. Rott[34], T. Ruhe[47], D. Ryckbosch[39], D. Rysewyk Cantu[35], I. Safa[10,16], S. E. Sanchez Herrera[35], A. Sandrock[47], J. Sandroos[18], M. Santander[43], S. Sarkar[55], S. Sarkar[44], K. Satalecka[2], M. Scharf[30], M. Schaufel[30], H. Schieler[8], P. Schlunder[47], T. Schmidt[26], A. Schneider[16], J. Schneider[13], F. G. Schröder[8,9], L. Schumacher[30], S. Sclafani[32], D. Seckel[9], S. Seunarine[56], S. Shefali[30], M. Silva[16], B. Skrzypek[10], B. Smithers[49], R. Snihur[16], J. Soedingrekso[47], D. Soldin[9], G. M. Spiczak[56], C. Spiering[2,61], J. Stachurska[2], M. Stamatikos[21], T. Stanev[9], R. Stein[2], J. Stettner[30], A. Steuer[18], T. Stezelberger[28], R. G. Stokstad[28], T. Stuttard[5], G. W. Sullivan[26], I. Taboada[33], F. Tenholt[23], S. Ter-Antonyan[41], S. Tilav[9], F. Tischbein[30], K. Tollefson[35], L. Tomankova[23], C. Tönnis[57], S. Toscano[4], D. Tosi[16], A. Trettin[2], M. Tselengidou[13], C. F. Tung[33], A. Turcati[24], R. Turcotte[8], C. F. Turley[12], J. P. Twagirayezu[35], B. Ty[16], M. A. Unland Elorrieta[31], J. Vandenbroucke[16], D. van Eijk[16], N. van Eijndhoven[37], D. Vannerom[14], J. van Santen[2], S. Verpoest[39], M. Vraeghe[39], C. Walck[6], A. Wallace[46], T. B. Watson[49], C. Weaver[35], A. Weindl[8], M. J. Weiss[12], J. Weldert[18], C. Wendt[16], J. Werthebach[47], M. Weyrauch[8], B. J. Whelan[46], N. Whitehorn[35,51], K. Wiebe[18], C. H. Wiebusch[30], D. R. Williams[43], M. Wolf[24], K. Woschnagg[19], G. Wrede[13], J. Wulff[23], X. W. Xu[41], Y. Xu[50], J. P. Yanez[44], S. Yoshida[45], T. Yuan[16], and Z. Zhang[50]

The IceCube Collaboration

[1] Department of Physics, Loyola University Chicago, Chicago, IL 60660, USA
[2] DESY, D-15738 Zeuthen, Germany
[3] Dept. of Physics and Astronomy, University of Canterbury, Private Bag 4800, Christchurch, New Zealand
[4] Université Libre de Bruxelles, Science Faculty CP230, B-1050 Brussels, Belgium
[5] Niels Bohr Institute, University of Copenhagen, DK-2100 Copenhagen, Denmark
[6] Oskar Klein Centre and Dept. of Physics, Stockholm University, SE-10691 Stockholm, Sweden
[7] Département de physique nucléaire et corpusculaire, Université de Genève, CH-1211 Genève, Switzerland
[8] Karlsruhe Institute of Technology, Institute for Astroparticle Physics, D-76021 Karlsruhe, Germany
[9] Bartol Research Institute and Dept. of Physics and Astronomy, University of Delaware, Newark, DE 19716, USA
[10] Department of Physics and Laboratory for Particle Physics and Cosmology, Harvard University, Cambridge, MA 02138, USA

[11] Department of Physics, Marquette University, Milwaukee, WI, 53201, USA
[12] Dept. of Physics, Pennsylvania State University, University Park, PA 16802, USA
[13] Erlangen Centre for Astroparticle Physics, Friedrich-Alexander-Universität Erlangen-Nürnberg, D-91058 Erlangen, Germany
[14] Dept. of Physics, Massachusetts Institute of Technology, Cambridge, MA 02139, USA
[15] Physics Department, South Dakota School of Mines and Technology, Rapid City, SD 57701, USA
[16] Dept. of Physics and Wisconsin IceCube Particle Astrophysics Center, University of Wisconsin–Madison, Madison, WI 53706, USA
[17] Dept. of Physics and Astronomy, University of California, Irvine, CA 92697, USA
[18] Institute of Physics, University of Mainz, Staudinger Weg 7, D-55099 Mainz, Germany
[19] Dept. of Physics, University of California, Berkeley, CA 94720, USA
[20] Dept. of Astronomy, Ohio State University, Columbus, OH 43210, USA
[21] Dept. of Physics and Center for Cosmology and Astro-Particle Physics, Ohio State University, Columbus, OH 43210, USA
[22] Dept. of Physics, University of Wuppertal, D-42119 Wuppertal, Germany
[23] Fakultät für Physik & Astronomie, Ruhr-Universität Bochum, D-44780 Bochum, Germany
[24] Physik-department, Technische Universität München, D-85748 Garching, Germany
[25] Dept. of Physics and Astronomy, University of Rochester, Rochester, NY 14627, USA
[26] Dept. of Physics, University of Maryland, College Park, MD 20742, USA
[27] Dept. of Physics and Astronomy, University of Kansas, Lawrence, KS 66045, USA
[28] Lawrence Berkeley National Laboratory, Berkeley, CA 94720, USA
[29] Dept. of Physics and Astronomy, Uppsala University, Box 516, SE-75120 Uppsala, Sweden
[30] III. Physikalisches Institut, RWTH Aachen University, D-52056 Aachen, Germany
[31] Institut für Kernphysik, Westfälische Wilhelms-Universität Münster, D-48149 Münster, Germany
[32] Dept. of Physics, Drexel University, 3141 Chestnut Street, Philadelphia, PA 19104, USA
[33] School of Physics and Center for Relativistic Astrophysics, Georgia Institute of Technology, Atlanta, GA 30332, USA
[34] Dept. of Physics, Sungkyunkwan University, Suwon 16419, Republic of Korea
[35] Dept. of Physics and Astronomy, Michigan State University, East Lansing, MI 48824, USA
[36] SNOLAB, 1039 Regional Road 24, Creighton Mine 9, Lively, ON, P3Y 1N2, Canada
[37] Vrije Universiteit Brussel (VUB), Dienst ELEM, B-1050 Brussels, Belgium
[38] Dept. of Astronomy and Astrophysics, Pennsylvania State University, University Park, PA 16802, USA
[39] Dept. of Physics and Astronomy, University of Gent, B-9000 Gent, Belgium
[40] Institut für Physik, Humboldt-Universität zu Berlin, D-12489 Berlin, Germany
[41] Dept. of Physics, Southern University, Baton Rouge, LA 70813, USA
[42] Dept. of Astronomy, University of Wisconsin–Madison, Madison, WI 53706, USA
[43] Dept. of Physics and Astronomy, University of Alabama, Tuscaloosa, AL 35487, USA
[44] Dept. of Physics, University of Alberta, Edmonton, Alberta, T6G 2E1, Canada
[45] Dept. of Physics and Institute for Global Prominent Research, Chiba University, Chiba 263-8522, Japan
[46] Department of Physics, University of Adelaide, Adelaide, 5005, Australia
[47] Dept. of Physics, TU Dortmund University, D-44221 Dortmund, Germany
[48] CTSPS, Clark-Atlanta University, Atlanta, GA 30314, USA
[49] Dept. of Physics, University of Texas at Arlington, 502 Yates St., Science Hall Rm 108, Box 19059, Arlington, TX 76019, USA
[50] Dept. of Physics and Astronomy, Stony Brook University, Stony Brook, NY 11794-3800, USA
[51] Department of Physics and Astronomy, UCLA, Los Angeles, CA 90095, USA
[52] Dept. of Physics, Yale University, New Haven, CT 06520, USA
[53] Department of Physics, Mercer University, Macon, GA 31207-0001, USA
[54] Dept. of Physics and Astronomy, University of Alaska Anchorage, 3211 Providence Dr., Anchorage, AK 99508, USA
[55] Dept. of Physics, University of Oxford, Parks Road, Oxford OX1 3PU, UK
[56] Dept. of Physics, University of Wisconsin, River Falls, WI 54022, USA
[57] Institute of Basic Science, Sungkyunkwan University, Suwon 16419, Republic of Korea
Received 2020 December 8; revised 2021 January 27; accepted 2021 January 27; published 2021 March 22

Abstract

In multi-messenger astronomy, rapid investigation of interesting transients is imperative. As an observatory with a 4π steradian field of view, and $\sim$99% uptime, the IceCube Neutrino Observatory is a unique facility to follow up transients, as well as to provide valuable insights for other observatories and inform their observational decisions. Since 2016, IceCube has been using low-latency data to rapidly respond to interesting astrophysical events reported by the multi-messenger observational community. Here, we describe the pipeline used to perform these followup analyses, and provide a summary of the 58 analyses performed as of July 2020. We find no significant signal in the first 58 analyses performed. The pipeline has helped inform various electromagnetic observation strategies, and has constrained neutrino emission from potential hadronic cosmic accelerators.

Unified Astronomy Thesaurus concepts: Neutrino astronomy (1100); High-energy astrophysics (739)

[58] also at Università di Padova, I-35131 Padova, Italy.
[59] also at National Research Nuclear University, Moscow Engineering Physics Institute (MEPhI), Moscow 115409, Russia.
[60] also at Earthquake Research Institute, University of Tokyo, Bunkyo, Tokyo 113-0032, Japan.
[61] also at National Research Nuclear University, Moscow Engineering Physics Institute (MEPhI), Moscow 115409, Russia.

1. Introduction

The recent successes of multi-messenger astronomy are due in large part to advancements in low-latency astronomical pipelines. Evidence for the first high-energy cosmic neutrino source, TXS 0506+056 (Aartsen et al. 2018a, 2018b), as well as the discovery of the first electromagnetic (EM) signal from a compact binary merger, GW170817, were both enabled by contemporaneous observations with various messengers (Abbott et al. 2017; Goldstein et al. 2017; Savchenko et al. 2017). Observations of this type are made possible by public channels, such as the Gamma-ray burst Coordinates Network (GCN)[62], and the Astronomer's Telegram (ATel)[63], which allow observers to coordinate observing strategies worldwide, and respond rapidly to interesting astrophysical transients.

Among the myriad of issues being investigated via real-time multi-messenger astronomy is the identification of cosmic neutrino sources. Generated from the decay of charged pions created in the course of proton-proton or photohadronic interactions in the vicinity of astrophysical accelerators, neutrinos serve as excellent messenger particles. Whereas cosmic rays are deflected on their journey to Earth, and the high-energy photons produced in both leptonic and hadronic processes are attenuated by extragalactic background light (EBL), neutrinos are neither deflected nor attenuated, and provide a smoking gun signature for hadronic acceleration.

However, the same small interaction probability which allows neutrinos to escape dense environments makes them notoriously difficult to detect. In addition, cosmic rays interacting within Earth's atmosphere produce showers of particles, including atmospheric muons and neutrinos, which comprise a large background when searching for astrophysical neutrinos. Despite these challenges, a diffuse astrophysical neutrino flux has been detected (Aartsen et al. 2016a, 2013a, 2014, 2020a; Schneider 2020; Stettner 2020), and has been described, using simple power laws, from energies of about 10 TeV to 10 PeV. Although evidence for a first high-energy neutrino source has been presented, it is estimated that any neutrino flux from the object TXS 0506+056 could account for no more than 1% of the total diffuse flux (Aartsen et al. 2020a).

In the search for astrophysical neutrino sources, the correlation of signals in multiple channels is crucial, as the aforementioned atmospheric backgrounds are often overwhelming. In fact, in analyses searching for steady neutrino point sources, when looking at the entire sky with no a priori list of candidate objects, no significant neutrino source has been detected over ten years of accumulated IceCube data (Aartsen et al. 2020b), as well as 11 years of ANTARES data (Aublin et al. 2019). It is not until neutrino data are correlated with lists of candidate neutrino emitters from EM observations that indications of neutrino signals from observed sources begin to manifest above the background expectation (Aartsen et al. 2020b). However, attempts to correlate astrophysical neutrinos with known sources thus far have fallen short of explaining diffuse flux, such as trying to correlate neutrinos with gamma-ray bursts (GRBs) (Aartsen et al. 2017a), gamma-ray detected blazars (Aartsen et al. 2017), fast radio bursts (FRBs) (Aartsen et al. 2020c, 2018c), the Galactic plane (Aartsen et al. 2017b), large-scale structures (Aartsen et al. 2020d; Fang et al. 2020), pulsar wind nebulae (Aartsen et al. 2020e), and the progenitors of gravitational waves (Albert et al. 2019, 2017; Aartsen et al. 2020f; ANTARES Collaboration et al. 2020; Hussain et al. 2020; Keivani et al. 2020). Many of these searches have set strong constraints on source classes which were once believed to be dominant sources of astrophysical neutrinos.

However, the similarity in energy densities between the diffuse astrophysical neutrino flux and the extragalactic gamma-ray background observed by the Fermi telescope (Ackermann et al. 2015) may be suggestive of common origins (Ahlers & Halzen 2018). The lack of a clear correlation in previous catalog searches may indicate that while this correspondence may not be straightforward, subclasses of previously investigated astrophysical sources could still be responsible for producing a significant fraction of the neutrino flux (Halzen et al. 2019). Moreover, evidence for neutrino emission clustered in time during the period 2014–2015 from TXS 0506+056 (Aartsen et al. 2018b) suggests that those extreme sources which may be neutrino emitters may also be variable in the time domain.

The identification of these extreme and variable sources is a problem well-suited to real-time observations. This was validated by the rigorous followup campaign of TXS 0506 +056, as the neutrino alert on 2017 September 22 (Aartsen et al. 2017c) set off a multi-wavelength followup of over 20 telescopes across gamma-ray, X-ray, optical, and radio wavelengths. While the identification of potential neutrino sources based on pointing EM telescopes in the direction of neutrino alerts has already proven fruitful, one can also trigger followups using neutrino data to search for emissions in the direction of EM objects while they are still in active states. This complementary approach provides another promising avenue for the identification of cosmic neutrino sources using real-time observations.

Here, we describe the fast-response analysis (hereafter FRA) pipeline, established to rapidly search for neutrino emission from interesting astrophysical transients, using data from the IceCube Neutrino Observatory. This pipeline has been running since 2016, and a subset of its results were shared publicly via channels such as GCN and ATel to help inform EM observation strategies. We begin by providing a brief description of the data sample in Section 2, and describe the analysis technique in Section 3. In Section 4, we explain the types of sources investigated via this pipeline. We summarize all of our results as of July 2020 in Section 5.

2. IceCube Data Sample

The IceCube Neutrino Observatory is a cubic-kilometer neutrino detector, installed at the geographic South Pole (Achterberg et al. 2006; Aartsen et al. 2017d). The detector consists of 5160 digital optical modules (DOMs), distributed on 86 strings, and buried at depths of between 1450 m and 2450 m. The DOMs consist of 10 inch photomultiplier tubes, onboard readout electronics, and a high-voltage board, all contained in a pressurized spherical glass container (Abbasi et al. 2009, 2010). In order to detect neutrinos, the DOMs are able to record Cherenkov radiation emitted by secondary particles produced by neutrino interactions in the surrounding ice or bedrock. Parameterization of the scattering and absorption of the glacial ice allows for accurate energy and the directional reconstruction of neutrino events (Aartsen et al. 2013b).

IceCube's field of view covers the whole sky with ∼99% uptime, although it is more sensitive to searches in the northern

[62] https://gcn.gsfc.nasa.gov/
[63] http://www.astronomerstelegram.org/

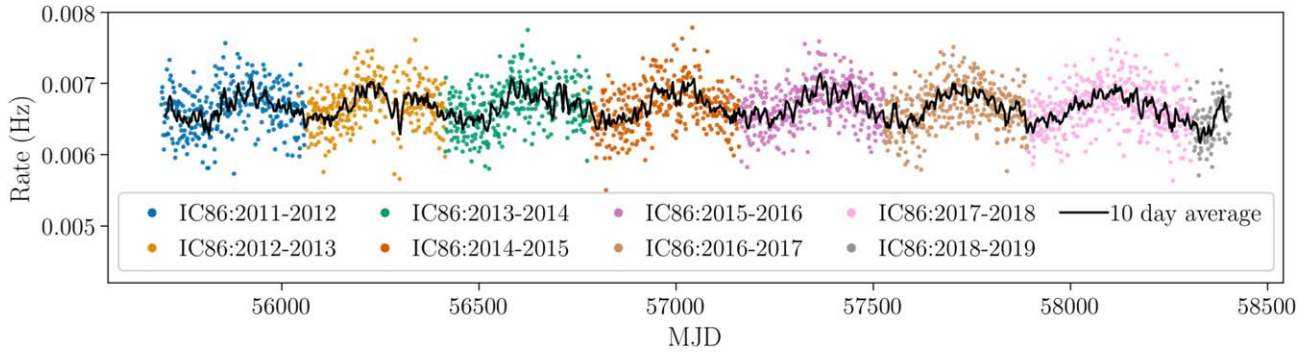

Figure 1. Rate of GFU event selection over time. Different detector operation seasons are denoted by different colors, where "IC86" denotes the full 86 string detector configuration for IceCube. Each data point is the rate calculated by averaging 3 sequential 8 hr "runs." As such, there is an expected Poissonian error for each data point, on the order of 5%, on the basis of statistical fluctuations only. In addition to this statistical fluctuation, the overall rate displays a clear annual modulation, whose peak-to-peak amplitude is approximately 4% of the mean rate. To balance the effects of statistics and this annual modulation, the background rate is estimated using a running average with a 10 day width (black), described more fully in Section 3.

celestial hemisphere, where the Earth attenuates the majority of the atmospheric muon signal. As such, the background at final selection level in the northern sky consists of atmospheric muon neutrinos from cosmic-ray air showers (Haack & Wiebusch 2018). In the southern sky, the trigger rate is dominated by atmospheric muons from cosmic-ray air showers, and harsher cuts are placed to reduce this overwhelming background.

Neutrino events in IceCube consist of two primary morphologies: tracks, and cascades. Tracks arise from charged-current ν_μ interactions, whereby the produced muon creates a long ($\mathcal{O}$(km)) straight Cherenkov light pattern throughout the detector. Cascades, on the other hand, come from neutral current interactions of any flavor, or charged-current $\nu_{e,\tau}$ interactions, and are characterized by spherical Cherenkov light patterns from particle showers. Whereas cascades have much better energy resolution, this analysis focuses on track-like events, as the long track topology not only provides an increased lever arm for better pointing resolution ($<1^\circ$ for $E_\nu > 10$ TeV), but also substantially increases the effective detection volume.

As this analysis runs in real time, it relies on the facility for rapid access to data from the South Pole. Specifics of the infrastructure established to construct a real-time neutrino event stream are detailed in Aartsen et al. (2017e). This system has previously been used to rapidly send alerts to optical, X-ray, and gamma-ray telescopes (Kintscher 2016), many of which have resulted in interesting EM observations (Abbasi et al. 2012; Evans et al. 2015; Aartsen et al. 2016b, 2015a). Here, we focus on data relating to extreme transients, taken from these EM observatories, to prompt searches of our own data. The specifics of the event selection used here, which we refer to as the "Gamma-ray Followup" (GFU) data set (owing to its initial application in sending alerts to gamma-ray facilities), is described in full in Aartsen et al. (2016b). The angular resolution of the sample as a function of energy is displayed in Aartsen et al. (2017e), Figure 4, and is very similar to other data sets that have been used for offline searches for neutrino sources (Aartsen et al. 2020b, Figure 1). At the final level, the stream has an all-sky rate that varies between approximately 6–7 mHz due to seasonal variations in the rate, and to atmospheric backgrounds (Desiati et al. 2011; Tilav et al. 2010; Grashorn et al. 2010). The variation of the sample's rate versus time is displayed in Figure 1, and our treatment of this modulation is described in Section 3. This rate is dominated in the northern hemisphere by atmospheric neutrinos, and in the southern hemisphere by atmospheric muons, but consists of $\mathcal{O}(0.1\%)$ ($\mathcal{O}(0.01\%)$) neutrino candidate events (hereafter referred to as events) from astrophysical ν_μ in the northern (southern) hemisphere.

3. Analysis Method

The FRA uses an unbinned maximum likelihood method, which is also a feature in other IceCube searches for neutrino point sources (Braun et al. 2008, 2010), and preliminary forms of this analytical method have been described in (Meagher et al. 2020; Meagher 2018). For a sample with N total neutrino candidate events in the analysis time window, we maximize the likelihood, $\mathcal{L}$, defined as

$$\mathcal{L}(n_s|n_b, \{x_i\}) = \frac{(n_s + n_b)^N e^{-(n_s+n_b)}}{N!} \times \prod_{i=1}^{N} \left[\frac{n_s}{n_s + n_b} \mathcal{S}(x_i) + \frac{n_b}{n_s + n_b} \mathcal{B}(x_i) \right], \quad (1)$$

with respect to n_s, where n_s and n_b are the signal and expected background event counts, respectively. The term outside of the product in the likelihood expression is introduced to help distinguish potential signal events in those regimes where the expected number of background events is small (Barlow 1990). Maximizing this "extended likelihood" with respect to only n_s has been a feature of previous IceCube analyses searching for short-timescale neutrino emission (Aartsen et al. 2017a, 2020c, 2020f). In Equation (1), the index i iterates over all neutrino event candidates, and $\mathcal{S}$ and $\mathcal{B}$ represent the signal and background probability density functions (PDFs) for events with observables x_i. The signal PDF, $\mathcal{S}$, is the product of both a spatial term, $\mathcal{S}_{\rm space}$, and an energy term, $\mathcal{S}_{\rm energy}$. The spatial term is modeled via a two-dimensional Gaussian:

$$\mathcal{S}_{\rm space} = \frac{1}{2\pi\sigma_i^2} e^{-\frac{|x_s - x_i|^2}{2\sigma_i^2}}, \quad (2)$$

using the event's reconstruction uncertainty σ_i for a source at location x_s. The energy term is used to distinguish backgrounds with a soft spectrum from signals with an assumed harder spectrum of $dN/dE \propto E^{-2}$. Thus, for each event, a PDF is evaluated, using the event's energy proxy, E_i, as well as its

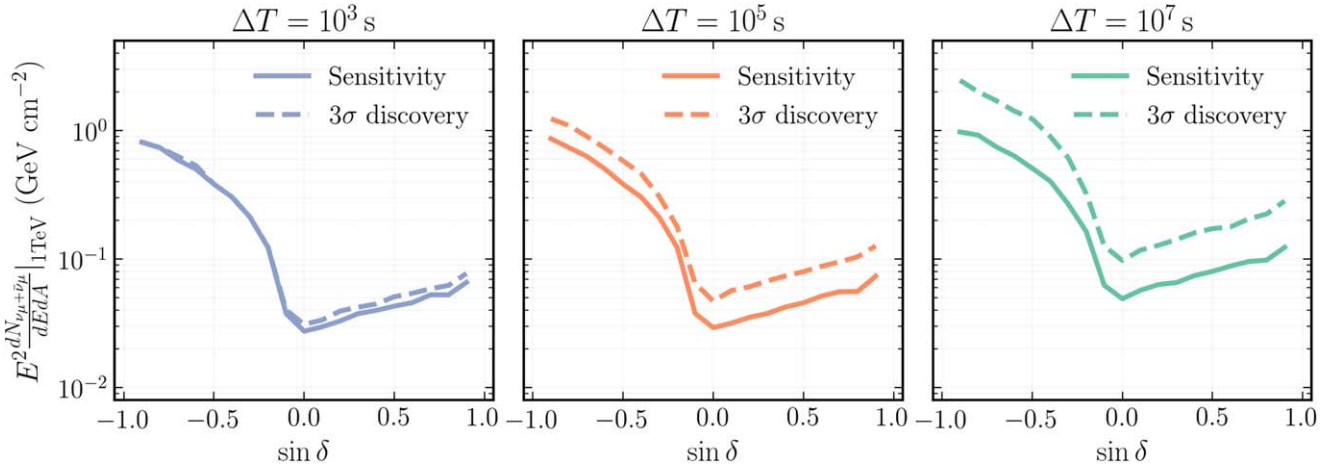

Figure 2. Analysis sensitivity as a function of declination (δ), for characteristic analysis timescales of 10^3 s (left), 10^5 s (middle), and 10^7 s (right), under the assumption of an E^{-2} power-law spectrum. Sensitivity (solid line) is defined as the median 90% CL upper limit that would be placed in the case of a non-detection, and discovery potential (dashed line) as the flux required to yield a 3σ significant result, pre-trials, in 90% of cases. The number of coincident neutrino candidate events increases as the time window for the analysis increases, which in turn increases the threshold for discovery. However, for time windows of less than about one day, well-reconstructed individual coincident neutrino candidate events are often capable of yielding analysis results that are significant at the 3σ level, pre-trials.

reconstructed declination, δ_i, as the effective area of the sample has a strong dependence on declination.

Similarly, the background PDF, $\mathcal{B}$, is the product of a spatial term, $\mathcal{B}_{\mathrm{space}}$, and an energy term, $\mathcal{B}_{\mathrm{energy}}$. $\mathcal{B}_{\mathrm{space}}$ is estimated using experimental data, and depends only on the event's declination, as the probability in R.A. is treated as a uniform distribution, $1/2\pi$. This yields

$$\mathcal{B}_{\mathrm{space}} = \mathcal{P}_{\mathcal{B}}(\sin\delta_i)/2\pi, \tag{3}$$

where $\mathcal{P}_{\mathcal{B}}$ is the PDF of the sample as a function of declination, determined directly from experimental data. The background energy term is a two-dimensional PDF, using the event's reconstructed declination and energy proxy, and is also determined directly from experimental data.

The final test statistic, $\mathcal{T}$, is twice the logarithm of the ratio between the likelihood, maximized with respect to n_s (best-fit value $\hat{n}_s$), and that of the background-only likelihood ($n_s = 0$). This simplifies to

$$\mathcal{T} = -2\hat{n}_s + 2\sum_{i=1}^{N} \ln\left[\frac{\hat{n}_s \mathcal{S}(x_i)}{n_b \mathcal{B}(x_i)} + 1\right], \tag{4}$$

In order to determine n_b, we calculate the average rate in data over a time window of 5 days' duration on either side of the time window being used for the analysis. For analyses being run in real time, there is often not 5 days' worth of data available after the end of the analysis time window; in this case, we use only the 5 days of data leading up to the start of the analysis. The duration of 5 days was chosen such that it balances the uncertainty in rate between two competing effects: (1) the Poissonian uncertainty from the number of events detected, and (2) the error from the fluctuating background rate due to seasonal variations, as discussed in Section 2. We then keep n_b fixed to this value, and only maximize the likelihood, $\mathcal{L}$, with respect to n_s.

The sensitivity of this analysis is dependent on the time window of the transient being investigated, as well as its location in the sky, and we show the sensitivity for various characteristic time windows, as well as different declinations, in Figure 2.

Sensitivities are defined on the assumption that the flux takes the form

$$\frac{dN_{\nu_\mu+\bar{\nu}_\mu}}{dEdAdt} = \phi_0 \times \left(\frac{E}{E_0}\right)^{-2}, \tag{5}$$

and is quoted in terms of the time-integrated flux, where $dN/dEdA = (dN/dEdAdt) \times \Delta T$, assuming constant emission. For short time windows, the analysis sensitivity is constant, as the expectation of a coincident event from background is significantly less than one. In this regime, a single signal event is enough to yield a significant result in the analysis. Figure 2 highlights the fact that the reduced background in the northern hemisphere significantly enhances analytical sensitivity.

The advantage of this analysis, in comparison with analyses which send alerts from IceCube, is that it reduces the threshold needed for a detection. Analyses which send neutrino alerts either require high-energy neutrino candidates (Blaufuss et al. 2020), where the effective area is smaller than in the GFU sample so as to only select premier candidates, or they require multiplets of lower-energy events in the GFU data (Kintscher 2016). This analysis, however, is sensitive to individual events that do not need to be of the same quality or energy as IceCube alert events. The response of this analysis to individual neutrino candidate events is displayed in Figure 3 for different power-law spectra, in terms of median pre-trials significance over many realizations. The significance is calculated by comparing the observed $\mathcal{T}$ to those based on pseudo-experiments, in which the times of the events are scrambled (Cassiday et al. 1989; Alexandreas et al. 1993). This temporal scrambling preserves detector acceptance as a function of declination, while altering the R.A., and times are reassigned in such a way as to preserve the observed seasonal variations discussed in Section 2. For time windows larger than a few hours, the effective area and background rate in the GFU sample are independent of R.A.. For shorter time windows, the slightly asymmetric azimuthal geometry of the detector leads to an effective area and background rate up to 10% higher for some right ascensions than others. Although this is not taken into account when calculating the signal and background PDFs, it does not introduce a bias in the calculation of the p-values reported in

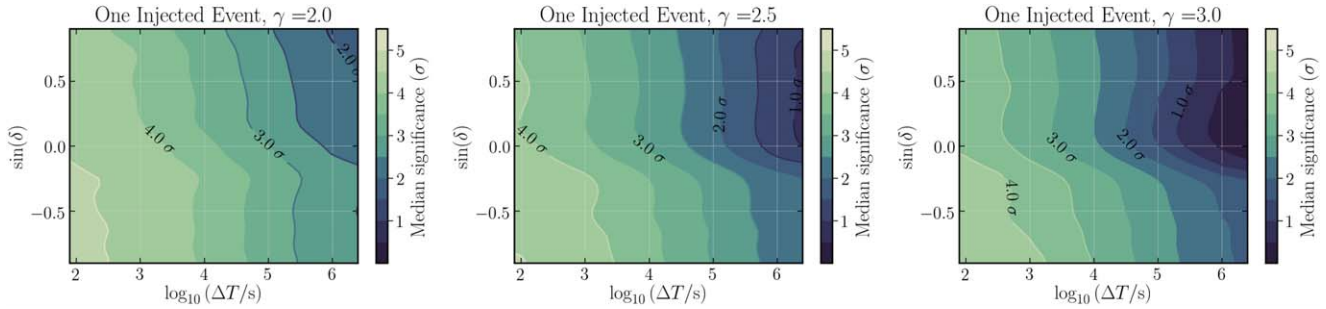

Figure 3. Statistical significance expected when detecting a signal neutrino candidate event. The color scale represents the median pre-trial significance for analyses, based on a variety of timescales and declinations when there is one signal event, sampled according to an $E^{-\gamma}$ power-law spectrum for $\gamma = 2.0$ (left), $\gamma = 2.5$ (middle), and $\gamma = 3.0$ (right), injected on top of a scrambled background. Although the analysis is designed for incident E^{-2} spectra, it remains sensitive to individual events from softer spectra. While a single event might result in a more significant result in the southern hemisphere than in the northern hemisphere, the analysis has a much smaller effective area in the southern hemisphere, and is thus less sensitive in this hemisphere.

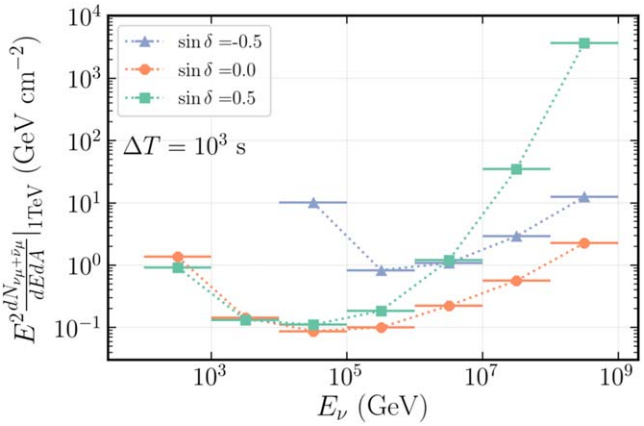

Figure 4. Differential sensitivity for an analysis with a 10^3 s time window, for a source in the northern sky (green), at the horizon (orange), or in the southern sky (blue). The sensitivities are calculated separately for each decade in terms of energy, assuming a differential muon neutrino flux $dN/dE \propto E^{-2}$ in that decade only. For events in the southern celestial hemisphere, the harsher cuts in the event selection render this analysis sensitive only at higher energies, whereas in the northern celestial hemisphere, the effect of Earth absorption is apparent in the highest energy bins.

this work, as the temporal scrambling preserves local coordinates, and thus maintains any azimuthal structure present in the sample.

Although the analysis is most sensitive to an incident E^{-2} flux, it remains capable of yielding significant results for sources with a softer spectrum. Whereas other searches for point sources often fit the spectral index of any potential signal, e.g., (Aartsen et al. 2020b), the index here is fixed, as we are looking for coincidences of individual events, from which it is not feasible to fit a spectrum.

As another way to highlight the analysis response to different spectral shapes, the differential sensitivity is provided in Figure 4. The analysis is most sensitive at the celestial equator and in the northern sky for energies between $\mathcal{O}(10^3)$ GeV and $\mathcal{O}(10^5)$ GeV, whereas in the southern sky, the harsher cuts increases this regime to around 10^6 GeV. For sources in the northern sky, Earth absorption becomes significant at the highest energies.

3.1. Sources with Localization Uncertainty

The analysis is also equipped to follow up sources where the uncertainty regarding the localization of the object is a significant fraction of the sky. This has applications in terms of searching for a variety of source classes, including, but not limited to, progenitors of gravitational waves, GRBs reported by the Fermi-GBM observatory, or poorly localized FRBs. In order to incorporate the localization uncertainty, the likelihood described in Equation (1) is maximized at every location in the sky, and the final test statistic is defined as

$$\Lambda = \max_{\alpha,\delta}\left[\mathcal{T}(\alpha,\,\delta) + 2\ln\left(\frac{P_s(\alpha,\,\delta)}{P_s(\alpha_0,\,\delta_0)}\right)\right], \tag{6}$$

where α and δ represent R.A. and declination, respectively. $P_s(\alpha,\,\delta)$ is the spatial PDF of the source being investigated, consisting of probabilities-per-pixel, with pixels corresponding to locations in the sky, generated according to the HEALPix scheme (Gorski et al. 2005). These PDFs are generally provided by whichever observatories initially detect the transient of interest. Here, α_0, and δ_0 denote the location in the sky, corresponding to the maximum of this PDF, and $\mathcal{T}$ is the test statistic defined in Equation (4). This technique has also been used in dedicated analyses searching for counterparts to gravitational wave progenitors (Aartsen et al. 2020f), ANITA neutrino candidates (Aartsen et al. 2020g), and ultra-high-energy cosmic rays (Schumacher 2019).

4. Follow-up Targets

In general, the FRA is run on extreme transients where there is potential for hadronic acceleration. In addition, this analytical method is used when it is believed that input from neutrino observations would be helpful in informing EM observing strategies. However, as the decision to perform the analysis is made on a case-by-case basis, it is difficult to define the exact circumstances that will result in an analysis. Potential targets predominately come from channels such as GCN or ATel, or are sometimes requested explicitly from EM observatories[64]. In general, we favor sources that are detected with high-energy EM emissions, and those sources which are in optimal locations for IceCube, i.e., sources at or above the celestial equator.

Once a potential target is identified, both the viability of the object's being a neutrino emitter, and the usefulness of input from a neutrino observatory for the EM community are evaluated. If it is decided to run the FRA, a time window, ΔT, is selected, which attempts to encompass interesting periods of

[64] Requests to perform the FRA can be sent to roc@icecube.wisc.edu.

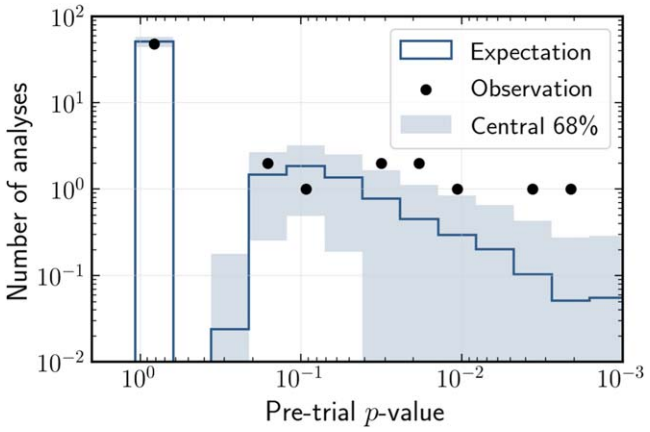

Figure 5. Distribution of p-values for all analyses. The p-values represent the outcome of each individual analysis, and do not include a trials correction for the ensemble of all analyses performed. As many of these analyses are looking for coincidences over short time windows, a large fraction of the analyses have zero coincident events, yielding $\mathcal{T} = 0$, and a p-value of exactly 1.0. We compare our distribution of p-values to those expected for many sets of ensembles of pseudo-experiments, based on scrambled background data for each of the 58 analyses performed.

EM emission (for example, covering the entirety of a period of flaring activity reported in a GCN or ATel), while remaining in a regime where the analysis is most sensitive. Once the analysis is complete, results are often shared via the channel where the emission prompting the analysis was discussed.

As of 2020 July, the FRA has been executed for a variety of astrophysical transients. While the analysis is designed to be applicable to generic objects, some classes of transients are followed up frequently (a complete list is provided in Appendix A). These classes include, but are not limited to: (1) extreme blazar flares, particularly those detected in extremely high energies, (2) bright GRBs, in particular the few detected by imaging air Cherenkov telescopes, (3) well-localized gravitational waves, (4) FRBs whose detections are released in real time, and (5) multi-messenger alert streams from the Astrophysical Multi-messenger observatory Network[65]. Since the pipeline's creation, some of these source classes, such as gravitational waves, have enjoyed dedicated real-time analyses (Aartsen et al. 2020f). Dedicated real-time follow-ups of GRBs, as well as the use of this pipeline to follow up neutrino candidate events sent by IceCube via AMON, will be the subjects of future works.

5. Results

As of July 2020, the FRA has been used to follow up external observations on 58 occasions. Although no analyses have resulted in significant results, we provide a complete list of those results in Table 1. The p-values are all quoted pre-trials, and the upper limits are set assuming an E^{-2} power law. For all analyses where $p < 0.01$, we provide skymaps of the analysis in Appendix B. A subset of these results were circulated via channels such as GCN or ATel, and links are provided where relevant. The distribution of all observed p-values is shown in Figure 5. The background distribution of p-values is not expected to be perfectly uniform, as many analyses operated at short timescales, where there are zero observed coincident events. In this case, $\mathcal{T} = 0$, and as this occurs for multiple pseudo-experiments, many pseudo-experiments yield the same value of $p = 1.0$. As the hypotheses tested for the individual followup analyses are unique, we do not attempt to make any statement regarding the collection of results as a population; instead, we highlight some of the analyses individually in Section 5.1.

For analyses where the p-value is not 1.0, we find that the test statistics are often dominated by one or two contributing neutrino candidate events. Although the analysis is capable of yielding significant results on the basis of one signal event from a hard astrophysical spectrum, none of our results are statistically significant, as all of the coincident events had low reconstructed energies.

Some results shared via GCN or ATel prior to the writing of this work show slight differences in p-value from those presented here, as they were performed using a preliminary version of this analytical method. The values provided in Table 1 are all calculated based on the analytical method described in Section 3. This version of the analysis has been stable since 2020 July, and continues to operate in real time.

5.1. Implications of Specific Analyses

Below, we highlight some of the objects that were analyzed. Following each source name, we include the declination of the object, as well as the time window for the analyses performed, as these are the principle factors driving the sensitivity of the analysis:

PKS 0346-27 ($\delta = -27.^{\circ}82$, $\Delta T = 4.2 \times 10^5$ s): The most significant result comes from an analysis of the object PKS 0346-27, a flat-spectrum radio quasar, with redshift $z = 0.991$. At the time of the analysis, the object was in a high state, marked by a daily averaged gamma-ray flux approximately 150 times greater than its four-year average, and with at least one photon with >30 GeV energy detected by the Fermi-LAT (ATel 11644). Our analysis found one event coincident with the localization of PKS 0346-27, yielding a p-value of 0.0027, before correcting for the number of analyses performed. However, after trials correcting for the number of analyses performed, we note that this most significant analysis has a post-trials p-value of 0.145, which we find to be consistent with background. Our upper limits, compared to observations across the EM spectrum at the time of the flare (Angioni et al. 2019), are displayed in Figure 6. Given that this source is located in the southern celestial hemisphere, we are only sensitive at the highest energies, owing to the strict cuts placed to reduce the harsh backgrounds in the southern sky.

AT 2018cow ($\delta = +22.^{\circ}27$, $\Delta T = 3.0 \times 10^5$ s): In recent years, time-domain optical surveys have revealed a growing class of rare and rapidly evolving extragalactic transients, or so-called "Fast Blue Optical Transients (FBOTs), see e.g., Rest et al. 2018; Drout et al. 2014; Arcavi et al. 2016. Among these objects is AT 2018cow, an object which prompted an extensive multi-wavelength followup campaign (Margutti et al. 2019). Early in the observations of the object, an FRA was run, under the assumption that the object could be a broad-lined Type Ic supernova, which has been considered as a potential source of astrophysical neutrinos (Tamborra & Ando 2016; Senno et al. 2016; Denton & Tamborra 2018). In this context, an analysis was performed over a 3 day time window, spanning the last optical non-detection to the first detection. Later observations of the object led to an array of possible classifications, including a tidal disruption event (TDE) or magnetar. In a

[65] https://gcn.gsfc.nasa.gov/amon.html

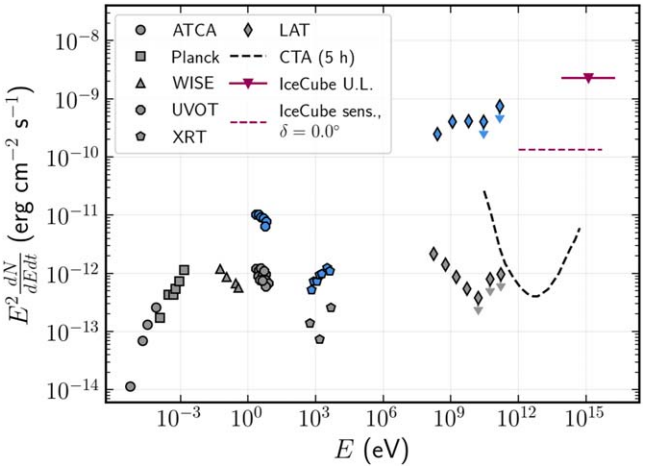

Figure 6. Spectral energy distribution of the flat-spectrum radio quasar, PKS 0346-27. All data points across the electromagnetic spectrum are taken from Angioni et al. (2019). Archival data are shown in gray, and data from 2018 May 16 are shown in blue. The limit placed by this analysis (solid magenta) uses a time window from 2018 May 11 to May 15, which covered the flaring activity on 2018 May 13, reported by the Fermi-LAT (ATel 11644). The May 16 time window for EM data points was selected based on the availability of synchronous Swift and Fermi-LAT data. For comparison, we show the potential sensitivity (dashed magenta line) of this analysis for the same observation time window, for a source at the horizon, where sensitivity is optimal. The energies for both our upper limit and sensitivity span the central 90% of the expected energies, assuming an E^{-2} flux. The black dashed line shows the sensitivity for CTA south over five hours of observations, and is taken from the Cherenkov Telescope Array Consortium et al. (2019).

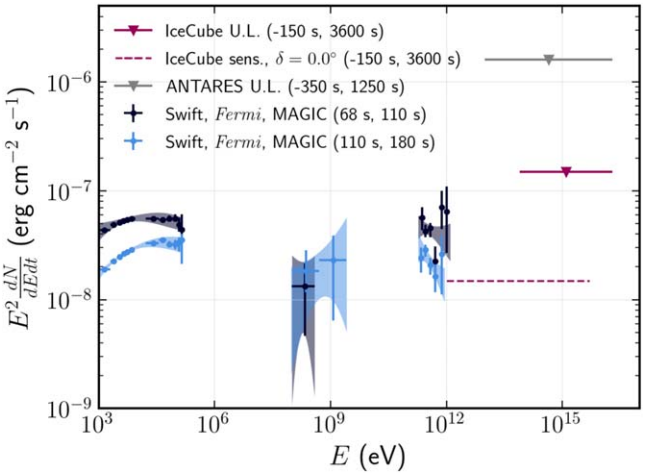

Figure 7. Multi-wavelength and multi-messenger spectra for GRB 190114C. Observation time windows are indicated in the legend. Neutrino upper limits are shown assuming an E^{-2} flux, and span the central 90% of the expected energies of neutrino events for this spectral assumption. The ANTARES limit is taken from Molla (2020). Data points across the electromagnetic spectrum are taken from Acciari et al. (2019b), and are shown for two time intervals. The lowest energy band represents the 90% confidence contours from a joint fit of Swift-BAT and Swift-XRT data, and the GeV and TeV bands are the 1σ contour regions from the best-fit power-law functions of Fermi-LAT and MAGIC, respectively. For comparison, we show the sensitivity (dashed magenta line) this analysis would have, based on the same observation time window, for a source at the horizon, where the sensitivity is optimal.

separate analysis, not part of the FRA program, the object was reanalyzed in the context of a potential TDE classification, implementing a time window from 30 days prior to peak, to 100 days after (Stein 2020). Although slight excesses were identified in both analyses, neither analysis was significant, even at the 3σ level, pre-trials. As such, we claim no evidence of neutrino emission, as neither analysis yielded statistically significant results. Magnetar-based models of this object which also predict neutrino emission are noted to be significantly below the sensitivity level of this analysis (Fang et al. 2019).

GRB 190114C ($\delta = -26.^{\circ}94$, $\Delta T = 3.8 \times 10^3$ s): This was the first GRB detected by an imaging air Cherenkov telescope to be announced in real time, with emissions in the 0.2–1.0 TeV band, detected by MAGIC (Acciari et al. 2019a). Although the high-energy peak in the broadband spectral energy distribution was later shown to be consistent with a synchrotron self-Compton interpretation (Acciari et al. 2019b), GRBs have long been thought of as potential sources of astrophysical neutrinos (Waxman & Bahcall 1997). While no coincident events were observed, the southern declination of this GRB places it in a location in the sky where the event selection places stringent cuts to reduce the atmospheric muon background; see Figure 4. As such, if there were neutrinos emitted at lower energies (less than $\mathcal{O}(10)$ TeV), the analysis would be much less sensitive than it would be for a similar source in the northern celestial hemisphere. The limits placed using this analysis are compared to the observations across the electromagnetic spectrum in Figure 7.

Given the redshift $z = 0.42$, and a corresponding luminosity distance of approximately 2.3 Gpc for GRB 190114C (Acciari et al. 2019b), we can also constrain the isotropic equivalent total radiated energy in muon neutrinos within our sensitive energy band, $E_{\nu,\mathrm{iso}}$. Using the upper limit presented in Table 1, we calculate

$$E_{\nu,\mathrm{iso}} = \frac{4\pi D_L(z)^2}{1+z} \int_{E_{5\%}}^{E_{95\%}} \frac{dN^{90\%}_{\nu_\mu+\bar{\nu}_\mu}}{dE_\nu\, dA} E_\nu dE_\nu, \tag{7}$$

where $E_{5\%}$ and $E_{95\%}$ represent the bounds on the central 90% of energies of detected events, assuming an E^{-2} spectrum, which, for this declination, we find to be around 100 TeV and 20 PeV, respectively. Accordingly, we constrain the total energy emitted in muon neutrinos within this energy range, assuming an E^{-2} spectrum, to be less than 1.6×10^{54} erg (90% CL). For comparison, the estimated isotropic energy emitted in photons was found to be around 3×10^{53} erg (Acciari et al. 2019b). A similar calculation could be performed for any object with a distance measurement as well as cataclysmic origins, investigated using the FRA. We have restricted our attention here to GRB 190114C owing to the extensive multi-wavelength observations of this object, and because it is one of the few GRBs detected at very high energies.

SGR 1935+2154/FRB 200428 ($\delta = +21.^{\circ}89$, $\Delta T = 8.6 \times 10^4$ s): In 2020 April, the CHIME/FRB instrument detected a millisecond timescale radio pulse, coincident with a period of extraordinarily intense X-ray burst activity from a known Galactic magnetar, SGR 1935+2154 (The CHIME/FRB Collaboration et al. 2020), which was also detected by STARE2 (Bochenek et al. 2020). Further analysis of the observables of this radio pulse, such as its duration and spectral luminosity, showed the signal to be indistinguishable from expectations for an FRB; this observation has supported the hypothesis that at least a fraction of the FRB population arise from magnetars (Bochenek et al. 2020). Both magnetars and FRBs have been proposed as possible cosmic-ray accelerators (Li et al. 2014; Gupta & Saini 2018; Metzger et al. 2020); as such, an analysis was performed

searching for coincident neutrino events. The time window (2020-04-27 18:00:00 UTC to 2020-04-28 18:00:00 UTC) began approximately half an hour prior to the Swift-BAT trigger (2020-04-27 18:26:20 UTC) and lasted for 24 hr, covering all available data at the time of the analysis, encompassing the observation time of FRB 200428 (2020-04-28 14:34:24.45), which occurred approximately 20 hr after the start of this window. One coincident neutrino candidate event, arriving during the period of bursting X-ray activity (2020-04-27 19:23:30.93 UTC), but significantly before the FRB, was identified. This event had a relatively large uncertainty with respect to its spatial reconstruction (2°.67 at 90% containment), and a low reconstructed energy of ∼1 TeV, resulting in an analysis p-value of 0.02 (which is not corrected for the ensemble of all analyses performed), which we find to be not statistically significant.

The results of this analysis, as well as other results from this pipeline, can be used to set limits on populations, using extreme objects identified by EM observations, as we highlight below.

Bochenek et al. (2020) showed that converting the detection of FRB 200428 to a volumetric rate of bursts results in an estimate of $7.23^{+8.78}_{-6.13} \times 10^7 \mathrm{Gpc}^{-3}\mathrm{yr}^{-1}$ for this type of transient, with an energy level greater than or equal to FRB 200428. We use this rate to set a constraint on the total contribution of FRBs from SGR 1935+2154-like bursts, assuming that for any neutrino flux, FRBs act as standard candles. An upper limit on this flux can be calculated using the technique outlined in Strotjohann (2020), i.e., by integrating the rate of sources times their individual flux contributions over cosmic history:

$$\frac{d\Phi}{dE} = \int_0^\infty R(z)\frac{dN}{dE}dz, \tag{8}$$

where $\frac{d\Phi}{dE}$ is the total diffuse differential flux from these bursts, and $\frac{dN}{dE}$ is the differential flux from each source. $R(z)$ is the rate at which transients appear on Earth, given by

$$R(z) = \rho(z) \times \frac{dV}{dz} \times \frac{1}{1+z}. \tag{9}$$

For the volumetric rate density, $\rho(z)$, we use the rate discussed above, and assume that FRBs track star formation activity, as given in Bochenek et al. (2020). The other term in the integrand in Equation (8) is calculated as

$$\frac{dN}{dE} = \frac{\mathcal{E}_{90\%}}{4\pi D_L^2} \times (1+z)^{3-\gamma}E^{-\gamma}, \tag{10}$$

where $\mathcal{E}_{90\%}$ is the upper limit on the time-integrated number of particles at 1 GeV in relation to the burst released in neutrinos, assuming the emission follows a spectral shape consistent with the diffuse astrophysical neutrino spectrum as reported in (Aartsen et al. 2015b). Although the likelihood used in the analysis assumes a spectral index of $\gamma = 2.0$, the analysis is still sensitive when we calculate this limit by injecting a softer flux, with a spectral index of $\gamma = 2.5$, as shown in Figure 3. To be conservative, we adopt a distance estimate for SGR 1935+2154 of 16 kpc, which was the maximal dispersion measure estimated distance reported in Bochenek et al. (2020). To calculate $\mathcal{E}_{90\%}$, we use the flux limit found using the FRA, as well as the distance of SGR 1935+2154. Our resulting limit, calculated using the public Flarestack code (Stein et al. 2020), is displayed in Figure 8, which compares this upper limit to the total observed diffuse astrophysical neutrino flux. For SGR 1935+2154, this corresponds to a limit on the energy of the burst of $\sim 4 \times 10^{43}$ erg, emitted between energies of 200 GeV and 80 TeV for a neutrino flux of the form $dN/dE \propto E^{-2.5}$. We find that, under the assumption that FRBs that track star formation activity and are standard candles in regards to their neutrino luminosities, a population of FRBs with the aforementioned rate can contribute no more than 0.3% of the diffuse neutrino flux.

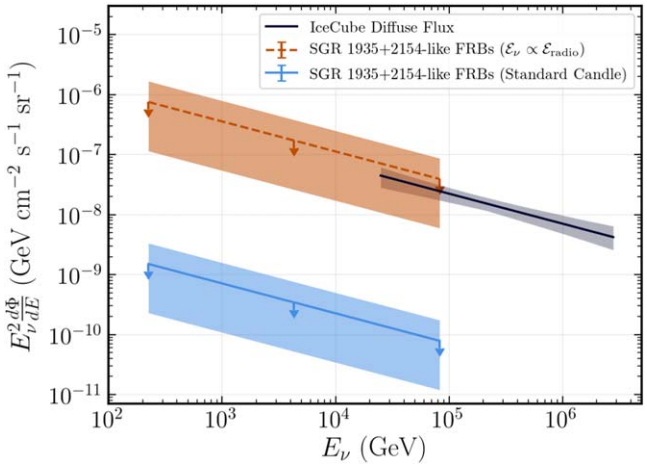

Figure 8. Upper limits on the contribution to the diffuse neutrino flux of a population of FRBs similar to SGR 1935+2154, for a variety of luminosity functions. The rate of such a population is taken from Bochenek et al. (2020), and the limit on neutrino luminosity is derived from our analysis of FRB 200428. For a naive standard candle assumption (light blue), the strict upper limit from the Galactic burst limits the contribution of FRBs to less than 1% of the diffuse astrophysical neutrino flux. However, if the emitted energy in neutrinos were to scale linearly with the energy emitted at radio wavelengths (dashed orange line), as described in the text, then FRBs are not ruled out as making a significant contribution to the diffuse neutrino flux. The band on each of these limits represents the uncertainty with respect to the reported volumetric rate of these transients.

While the majority of the detected FRB population is extragalactic, a non-detection of a Galactic FRB implies an extremely small flux from extragalactic FRBs, under the assumption of standard candles. If, instead of assuming equal neutrino luminosities, the neutrino contribution were to scale linearly with the emitted radio energy, this constraint would scale by the ratio of the mean FRB energy to that from FRB 200428. If one assumes that the volumetric rate of FRBs per unit isotropic energy scales, according to a power-law distribution, $dN/d\mathcal{E} \propto \mathcal{E}^{-\gamma}$, where $\gamma = 1.7$, and extends from the spectral energy of FRB 200428 out to a maximal spectral energy, $\mathcal{E}_{\rm max} \approx 2 \times 10^{33}$erg Hz^{-1} (Lu & Piro 2019), then this ratio of spectral energies is on the order of 5×10^2. Rescaling our upper limit for the total FRB contribution to diffuse neutrino flux would then overshoot the total astrophysical neutrino flux, implying that if a population of SGR 1935+2154-like FRBs are not neutrino standard candles, and instead represent a positive correlation between neutrino and radio luminosities, then there is still room for them to contribute significantly to the diffuse neutrino flux. Even so, this limit highlights the fact that this pipeline can be used to constrain populations of potential neutrino sources by analyzing the most extreme objects identified in EM observations.

6. Discussion and Conclusion

We have presented a pipeline for rapidly investigating neutrino data in searches for extreme astrophysical transients. This analysis is well-suited to searching for individual

coincident neutrinos with objects detected using other messengers. Since its inception in 2016, this pipeline has proven useful in informing EM observers about possible neutrino emission, and has helped develop observational strategies. As of 2020 July, no analyses have yet resulted in significant detections. Our limits have helped constrain various models of hadronic acceleration for a number of source classes that are thought to be cosmic-ray accelerators, including, but not limited to, superluminous transients, such as AT 2018cow, and Galactic magnetars. The pipeline will continue to be operational. Beginning in 2018, this pipeline has circulated more of its results in real time via channels such as ATel or GCN, as is evident in Table 1. This has proven useful in aiding EM observational decisions, and these results have also been used by those creating lepto-hadronic emission models of certain transients of great interest to the observational community, such as AT 2018cow (Fang et al. 2019).

With its 4π steradian field of view and $\sim$99% uptime, IceCube is a unique observatory, in that it is able to report on nearly every astrophysical transient. The ability to rapidly communicate a neutrino detected from an astrophysical transient enables the observational community to observe interesting objects when they are still in states of outburst, which could be pivotal in terms of understanding the nature of astrophysical neutrinos.

The IceCube Collaboration acknowledges the significant contributions to this manuscript made by Alex Pizzuto and Justin Vandenbroucke. The authors gratefully acknowledge support from the following agencies and institutions: USA–the U.S. National Science Foundation–Office of Polar Programs, the U.S. National Science Foundation–Physics Division, Wisconsin Alumni Research Foundation, the Center for High Throughput Computing (CHTC) at the University of Wisconsin–Madison, the Open Science Grid (OSG), Extreme Science and Engineering Discovery Environment (XSEDE), the Frontera computing project at the Texas Advanced Computing Center, the U.S. Department of Energy–National Energy Research Scientific Computing Center, the Particle astrophysics research computing center at the University of Maryland, the Institute for Cyber-Enabled Research at Michigan State University, and the Astroparticle physics computational facility at Marquette University; Belgium–Funds for Scientific Research (FRS-FNRS and FWO), the FWO Odysseus and Big Science programmes, and the Belgian Federal Science Policy Office (Belspo); Germany–Bundesministerium für Bildung und Forschung (BMBF), Deutsche Forschungsgemeinschaft (DFG), the Helmholtz Alliance for Astroparticle Physics (HAP), the Initiative and Networking Fund of the Helmholtz Association, Deutsches Elektronen Synchrotron (DESY), and the High Performance Computing cluster of the RWTH, Aachen; Sweden–the Swedish Research Council, the Swedish Polar Research Secretariat, the Swedish National Infrastructure for Computing (SNIC), and the Knut and Alice Wallenberg Foundation; Australia–the Australian Research Council; Canada–the Natural Sciences and Engineering Research Council of Canada, Calcul Québec, Compute Ontario, the Canada Foundation for Innovation, WestGrid, and Compute Canada; Denmark–the Villum Fonden and Carlsberg Foundation; New Zealand–the Marsden Fund; Japan–the Japan Society for the Promotion of Science (JSPS), and the Institute for Global Prominent Research (IGPR) of Chiba University; Korea–the National Research Foundation of Korea (NRF); Switzerland–the Swiss National Science Foundation (SNSF); United Kingdom–the Department of Physics, University of Oxford.

Software: Flarestack (Stein et al. 2020), astropy (Price-Whelan et al. 2018), numpy (Van der Walt et al. 2011), scipy (Virtanen et al. 2020) matplotlib (Hunter 2007), pandas (McKinney 2010).

Appendix A
List of Results

Table 1 contains information on all of the analyses performed as of 2020 July. References are provided to the GCN or ATel that prompted the analyses, although many of these objects were the topic of multiple GCN circulars or ATels.

Table 1
Results of All Fast-Response Analyses to Date

Source Name	R.A. (°)	dec. (°)	Start time (UTC)	Duration (s)	$\hat{n}_s$	$-\log_{10}(p)$	Upper limit (GeV cm^{-2})	Energy Range (GeV)	Reference	IceCube Response
Cygnus X-3	308.11	+40.96	2017-04-03 00:00:00.000	8.64×10^4	0.00	0.00	5.2×10^{-2}	$(7 \times 10^2, 4 \times 10^5)$	ATel 10243	⋯
GRB 170405A	219.83	−25.24	2017-04-05 18:35:49.000	1.20×10^3	0.00	0.00	3.2×10^{-1}	$(7 \times 10^4, 2 \times 10^7)$	GCN 20987	⋯
AGL J0523+0646	80.86	+6.78	2017-04-15 11:50:00.000	4.32×10^5	0.00	0.00	3.9×10^{-2}	$(1 \times 10^3, 3 \times 10^6)$	ATel 10282	⋯
AT 2017eaw	308.68	+60.19	2017-05-10 12:00:00.000	2.59×10^5	0.23	0.89	7.4×10^{-2}	$(6 \times 10^2, 2 \times 10^5)$	ATel 10372	⋯
Fermi J1544-0649	236.08	−6.82	2017-05-15 00:00:00.000	2.74×10^5	0.00	0.00	5.1×10^{-2}	$(2 \times 10^3, 9 \times 10^6)$	ATel 10482	⋯
Fermi J1544-0649	236.08	−6.82	2017-05-18 04:04:40.000	9.36×10^5	0.00	0.00	5.6×10^{-2}	$(2 \times 10^3, 9 \times 10^6)$	ATel 10482	⋯
AXP 4U 0142+61	26.59	+61.75	2017-07-13 22:54:33.000	7.20×10^3	0.00	0.00	5.9×10^{-2}	$(5 \times 10^2, 2 \times 10^5)$	GCN 21342	⋯
GRB 170714A	34.35	+1.99	2017-07-14 11:25:32.000	4.36×10^4	0.00	0.00	3.0×10^{-2}	$(1 \times 10^3, 5 \times 10^6)$	GCN 21345	⋯
AT 2017fro	259.98	+41.68	2017-07-22 00:00:00.000	1.21×10^6	0.00	0.00	6.1×10^{-2}	$(7 \times 10^2, 3 \times 10^5)$	ATel 10652	⋯
AGL J1412-0522	213.00	−5.40	2017-08-05 03:00:00.000	1.73×10^5	0.00	0.00	4.0×10^{-2}	$(2 \times 10^3, 8 \times 10^6)$	ATel 10623	⋯
G298048 SSS17a	197.45	−23.38	2017-08-17 12:32:44.000	1.00×10^3	0.00	0.00	3.1×10^{-1}	$(7 \times 10^4, 2 \times 10^7)$	GCN 21529	⋯
G298048 SSS17a	197.45	−23.38	2017-08-17 12:41:04.000	1.21×10^6	0.00	0.00	3.2×10^{-1}	$(7 \times 10^4, 2 \times 10^7)$	GCN 21529	⋯
TXS 0506+056	77.36	+5.69	2017-09-15 00:00:00.000	1.21×10^6	0.00	0.00	3.9×10^{-2}	$(1 \times 10^3, 3 \times 10^6)$	ATel 10791[a]	⋯
PKS 0131-522	23.27	−52.00	2017-11-16 00:00:00.000	1.73×10^5	0.77	1.39	1.1×10^0	$(9 \times 10^4, 2 \times 10^7)$	ATel 10987	⋯
GRB 171205A	167.41	−12.59	2017-12-05 06:20:43.000	7.20×10^3	0.00	0.00	1.4×10^{-1}	$(2 \times 10^4, 2 \times 10^7)$	GCN 22177	⋯
Mrk 421	166.11	+38.21	2017-12-19 00:00:00.000	1.73×10^5	0.00	0.00	5.5×10^{-2}	$(7 \times 10^2, 4 \times 10^5)$	ATel 11077	⋯
Mrk 421	166.11	+38.21	2018-01-12 00:00:00.000	8.64×10^5	0.00	0.00	5.9×10^{-2}	$(7 \times 10^2, 4 \times 10^5)$	⋯	⋯
HESS J0632+057	98.25	+5.80	2018-01-17 00:00:00.000	6.05×10^5	0.00	0.00	3.3×10^{-2}	$(1 \times 10^3, 3 \times 10^6)$	ATel 11223	⋯
CXOU J16740.2-455216	251.79	−45.87	2018-02-05 18:27:11.000	6.88×10^4	0.00	0.00	6.3×10^{-1}	$(9 \times 10^4, 2 \times 10^7)$	ATel 11264	⋯
Sgr A*	266.42	−29.01	2018-02-17 00:30:00.000	1.80×10^3	0.00	0.00	3.7×10^{-1}	$(8 \times 10^4, 2 \times 10^7)$	ATel 11313	⋯
TXS 0506+056	77.36	+5.69	2018-03-09 00:00:00.000	5.53×10^5	0.00	0.00	3.6×10^{-2}	$(1 \times 10^3, 3 \times 10^6)$	ATel 11419	⋯
FSRQ 3C 279	194.05	−5.79	2018-04-15 00:00:00.000	3.02×10^5	0.00	0.00	3.8×10^{-2}	$(2 \times 10^3, 8 \times 10^6)$	ATel 11545	⋯
PKS 0346-27	57.16	−27.82	2018-05-11 00:00:00.000	4.18×10^5	0.98	2.57	5.9×10^{-1}	$(8 \times 10^4, 2 \times 10^7)$	ATel 11644	⋯
PKS 0903-57	136.22	−57.58	2018-05-12 00:00:00.000	3.31×10^5	0.00	0.00	8.1×10^{-1}	$(1 \times 10^5, 2 \times 10^7)$	ATel 11644	⋯
AT 2018cow	244.00	+22.27	2018-06-13 00:00:00.172	2.97×10^5	1.19	1.64	5.9×10^{-2}	$(8 \times 10^2, 8 \times 10^5)$	ATel 11727	ATel 11785
2FHL J1037.6+5710	159.41	+57.17	2018-06-29 21:59:00.000	1.69×10^5	0.62	1.08	8.3×10^{-2}	$(6 \times 10^2, 2 \times 10^5)$	ATel 11806	⋯
NVSS J163547+362930	248.95	+36.49	2018-07-06 12:00:00.000	3.46×10^5	0.00	0.00	9.6×10^{-2}	$(7 \times 10^2, 4 \times 10^5)$	ATel 11847	⋯
FRB 180725A	6.22	+67.05	2018-07-25 05:59:43.115	8.64×10^4	0.00	0.00	7.7×10^{-2}	$(5 \times 10^2, 1 \times 10^5)$	ATel 11901	⋯
GRB 180728A	253.57	−54.03	2018-07-28 16:29:00.073	7.20×10^3	0.00	0.00	7.3×10^{-1}	$(9 \times 10^4, 2 \times 10^7)$	GCN 23046	⋯
IGR J17591-2342	269.79	−23.71	2018-08-10 12:00:00.000	1.50×10^6	0.00	0.00	3.2×10^{-1}	$(7 \times 10^4, 2 \times 10^7)$	ATel 12004	⋯
FSRQ 4C +38.41	248.82	+38.41	2018-09-01 09:00:00.000	2.59×10^5	0.00	0.00	5.2×10^{-2}	$(7 \times 10^2, 4 \times 10^5)$	ATel 12005	⋯
HAWC All-Sky Flare Alert	101.82	+37.61	2018-09-02 11:22:30.000	1.95×10^5	0.00	0.00	5.1×10^{-2}	$(7 \times 10^2, 4 \times 10^5)$	⋯	⋯
AT 2018gep	250.95	+41.05	2018-09-08 04:00:00.000	1.42×10^6	1.61	1.46	1.2×10^{-1}	$(7 \times 10^2, 4 \times 10^5)$	ATel 12030	ATel 12062
GRB 180914A	52.74	−5.26	2018-09-14 11:31:47.000	7.20×10^3	0.00	0.00	3.3×10^{-2}	$(2 \times 10^3, 8 \times 10^6)$	GCN 23225	⋯
GRB 180914B	332.45	+24.88	2018-09-14 18:22:00.000	4.80×10^2	0.00	0.00	3.8×10^{-2}	$(8 \times 10^2, 7 \times 10^5)$	GCN 23226	⋯
Crab Nebula	83.63	+22.01	2018-09-30 00:00:00.000	1.03×10^6	0.00	0.00	5.4×10^{-2}	$(8 \times 10^2, 9 \times 10^5)$	ATel 12095	⋯
SDSS J00289.81+200026.7	7.12	+20.00	2018-10-03 12:00:00.000	3.02×10^5	0.00	0.00	4.0×10^{-2}	$(8 \times 10^2, 1 \times 10^6)$	ATel 12084	⋯
Fermi J1153-1124	178.30	−11.11	2018-11-10 00:00:00.000	1.73×10^5	0.97	2.40	1.6×10^{-1}	$(9 \times 10^3, 1 \times 10^7)$	ATel 12206	ATel 12210
TXS 0506+056	77.35	+5.70	2018-11-27 00:00:00.000	6.05×10^5	0.00	0.00	3.7×10^{-2}	$(1 \times 10^3, 3 \times 10^6)$	ATel 12260	ATel 12267
GRB 190114C	54.51	−26.94	2019-01-14 20:54:33.000	3.78×10^3	0.00	0.00	3.5×10^{-1}	$(8 \times 10^4, 2 \times 10^7)$	ATel 12390	ATel 12395
Mrk 421	166.08	+38.19	2019-04-08 00:00:01.000	1.43×10^6	0.00	0.00	6.4×10^{-2}	$(7 \times 10^2, 4 \times 10^5)$	ATel 12680	⋯
ANTARES-LAT coincidence	46.18	−8.27	2019-05-12 01:26:13.000	2.00×10^3	0.00	0.00	6.7×10^{-2}	$(3 \times 10^3, 1 \times 10^7)$	⋯	⋯
FRB 190711	329.00	−80.38	2019-07-10 13:53:41.100	8.64×10^4	0.00	0.00	1.1×10^0	$(9 \times 10^4, 2 \times 10^7)$	ATel 12922	ATel 12928
FRB 190711	329.00	−80.38	2019-07-11 01:52:01.100	2.00×10^2	0.00	0.00	1.0×10^0	$(9 \times 10^4, 2 \times 10^7)$	ATel 12922	ATel 12928
FRB 190714	183.97	−13.00	2019-07-13 17:37:12.901	8.64×10^4	0.00	0.00	1.5×10^{-1}	$(2 \times 10^4, 2 \times 10^7)$	ATel 12940	ATel 12956
FRB 190714	183.97	−13.00	2019-07-14 05:35:32.901	2.00×10^2	0.00	0.00	1.4×10^{-1}	$(2 \times 10^4, 2 \times 10^7)$	ATel 12940	ATel 12956
HAWC Burst Alert	78.39	+6.61	2019-08-06 07:20:48.000	4.32×10^4	0.00	0.00	3.5×10^{-2}	$(1 \times 10^3, 3 \times 10^6)$	GCN Notice	GCN 25291

Table 1
(Continued)

Source Name	R.A. (°)	dec. (°)	Start time (UTC)	Duration (s)	$\hat{n}_s$	$-\log_{10}(p)$	Upper limit (GeV cm^{-2})	Energy Range (GeV)	Reference	IceCube Response
S190814bv	13.95	−27.08	2019-08-14 18:46:39.010	1.22×10^6	0.00	0.00	3.8×10^{-1}	$(8 \times 10^4, 2 \times 10^7)$	GCN 25487	GCN 25557
GRB 190829A	44.54	−8.97	2019-08-29 19:55:43.000	9.00×10^1	0.00	0.00	8.5×10^{-2}	$(4 \times 10^3, 1 \times 10^7)$	GCN 25552	⋯
GRB 190829A	44.54	−8.97	2019-08-29 19:55:53.000	8.64×10^4	0.00	0.00	8.7×10^{-2}	$(4 \times 10^3, 1 \times 10^7)$	GCN 25552	⋯
HAWC-190917A	321.84	+30.97	2019-09-16 19:14:19.000	4.32×10^4	0.93	1.85	6.0×10^{-2}	$(7 \times 10^2, 5 \times 10^5)$	GCN 25766	GCN 25775
1ES 2344+51.4	356.77	+51.71	2019-10-01 00:00:01.000	5.18×10^5	0.00	0.00	7.0×10^{-2}	$(6 \times 10^2, 3 \times 10^5)$	ATel 13165	⋯
PKS 2004-447	301.98	−44.58	2019-10-22 12:00:00.000	5.18×10^5	0.00	0.00	6.0×10^{-1}	$(9 \times 10^4, 2 \times 10^7)$	ATel 13229	ATel 13249
SBS 1150+497	178.35	+49.52	2019-10-30 00:00:01.000	1.73×10^5	0.07	0.79	5.7×10^{-2}	$(6 \times 10^2, 3 \times 10^5)$	ATel 13253	ATel 13266
ANTARES-LAT coincidence	240.45	−52.96	2020-01-26 18:52:02.950	1.73×10^5	0.00	0.00	7.5×10^{-1}	$(9 \times 10^4, 2 \times 10^7)$	GCN 26915	GCN 26922
VER J0521+211	80.44	+21.21	2020-02-25 02:52:48.000	8.64×10^4	0.00	0.00	4.0×10^{-2}	$(8 \times 10^2, 9 \times 10^5)$	ATel 13522	ATel 13532
PKS 0903-57	136.22	−57.59	2020-03-24 12:00:00.000	1.81×10^6	0.00	0.00	7.5×10^{-1}	$(1 \times 10^5, 2 \times 10^7)$	ATel 13632	⋯
SGR 1935+2154	293.74	+21.89	2020-04-27 18:00:00.000	8.64×10^4	0.83	1.62	5.5×10^{-2}	$(8 \times 10^2, 9 \times 10^5)$	ATel 13675	ATel 13689

Note. p-values are not trials-corrected for the number of analyses performed. Upper limits are placed at the 90% CL under the assumption of an E^{-2} flux, and constrain the energy-scaled time-integrated flux, $E^2 dN/dEdA$. The energy range column denotes the central 90% of the energies expected for signal events from a source at a given declination, under the assumption of an E^{-2} flux. Locations in the sky are quoted for the J2000 epoch. Analyses with no listed reference were triggered by private communications.

[a] The analysis of TXS 0506+056 reported by Fermi-LAT in this ATel was prompted by IceCube-170922A, an IceCube event sent as a public alert. This event was excluded from the FRA analysis here.

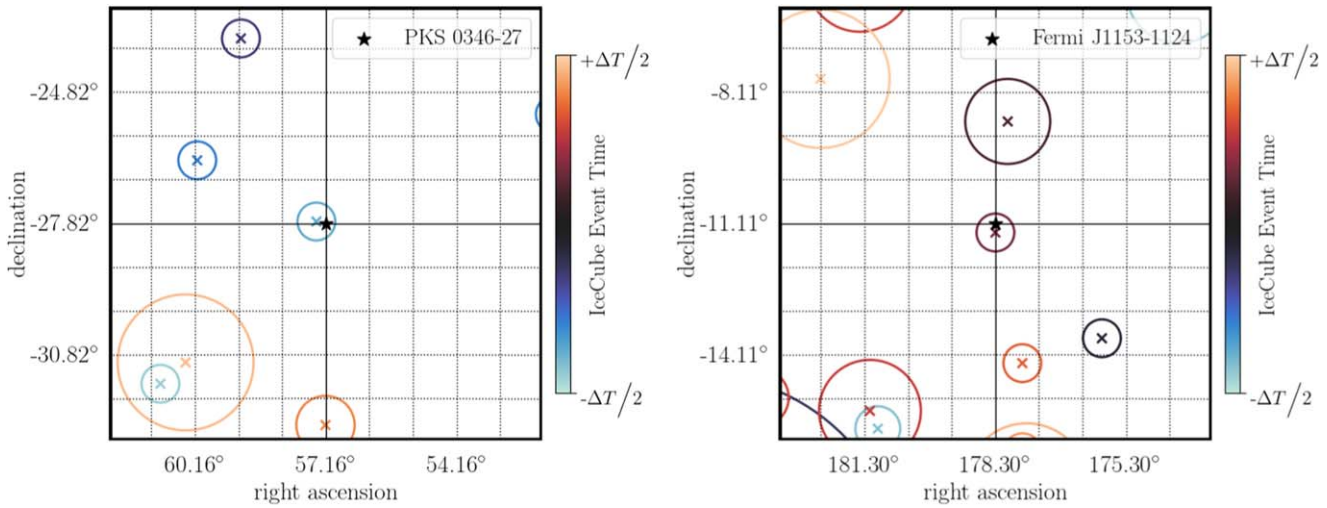

Figure 9. Skymaps for the two analyses resulting in a p-value of less than 0.01, pre-trials. Maps are centered on the location of the source under investigation. Each colored × represents a neutrino candidate event in the GFU sample, where the color represents the arrival time of the event, and the size of the circle is each event's angular uncertainty (90% containment). The analysis for PKS 0346-27 (left) lasted four days, and included a period of increased gamma-ray emission, detected by Fermi-LAT, and the analysis of a newly detected gamma-ray source, Fermi J1153-1124 (right), was of 2 days' duration.

Appendix B
Skymaps

In Figure 9, we present skymaps of all analyses resulting in a p-value less than 0.01, pre-trials, although we note that after trials corrections, our most significant result is consistent with background, with a trials-corrected p-value of 0.145. These analyses include (1) the followup of a bright GeV flare reported by the Fermi-LAT from the blazar PKS 0346-27, and (2) Fermi J1153-1124, a source which, at the time, was a newly-identified gamma-ray source.

ORCID iDs

M. Ahlers https://orcid.org/0000-0003-0709-5631
S. BenZvi https://orcid.org/0000-0001-5537-4710
E. Bernardini https://orcid.org/0000-0003-3108-1141
F. Bradascio https://orcid.org/0000-0002-7750-5256
S. Bron https://orcid.org/0000-0002-6305-3041
P. Coppin https://orcid.org/0000-0001-6869-1280
P. Correa https://orcid.org/0000-0002-1158-6735
J. C. Díaz-Vélez https://orcid.org/0000-0002-0087-0693
M. A. DuVernois https://orcid.org/0000-0002-2987-9691
A. Franckowiak https://orcid.org/0000-0002-5605-2219
F. Halzen https://orcid.org/0000-0001-6224-2417
A. Kappes https://orcid.org/0000-0003-1315-3711
U. Katz https://orcid.org/0000-0002-7063-4418
H. Kolanoski https://orcid.org/0000-0003-0435-2524
H. Niederhausen https://orcid.org/0000-0002-9566-4904
M. U. Nisa https://orcid.org/0000-0002-6859-3944
H. Pandya https://orcid.org/0000-0002-6138-4808
A. Pizzuto https://orcid.org/0000-0002-8466-8168
W. Rhode https://orcid.org/0000-0003-2636-5000
B. Riedel https://orcid.org/0000-0002-9524-8943
D. Ryckbosch https://orcid.org/0000-0002-8759-7553
K. Satalecka https://orcid.org/0000-0002-7669-266X
L. Schumacher https://orcid.org/0000-0001-8945-6722
K. Tollefson https://orcid.org/0000-0001-9725-1479
J. Weldert https://orcid.org/0000-0002-3709-2354
N. Whitehorn https://orcid.org/0000-0002-3157-0407

References

Aartsen, M. G., Abbasi, R., Abdou, Y., et al. 2013a, Sci, 342, 1242856
Aartsen, M. G., Abbasi, R., Abdou, Y., et al. 2013b, NIMPA, 711, 73
Aartsen, M. G., Abraham, K., Ackermann, M., et al. 2015a, ApJ, 811, 52
Aartsen, M. G., Abraham, K., Ackermann, M., et al. 2015b, ApJ, 809, 98
Aartsen, M. G., Abraham, K., Ackermann, M., et al. 2016a, ApJ, 833, 3
Aartsen, M. G., Abraham, K., Ackermann, M., et al. 2016b, JINST, 11, P11009
Aartsen, M. G., Abraham, K., Ackermann, M., et al. 2017b, ApJ, 849, 67
Aartsen, M. G., Abraham, K., Ackermann, M., et al. 2017c, GCN Circ., 21916 https://gcn.gsfc.nasa.gov/gcn3/21916.gcn3
Aartsen, M. G., Abraham, K., Ackermann, M., et al. 2017d, JINST, 12, P03012
Aartsen, M. G., Abraham, K., Ackermann, M., et al. 2017e, APh, 92, 30
Aartsen, M. G., Abraham, K., Ackermann, M., et al. 2018a, Sci, 361, eaat1378
Aartsen, M. G., Abraham, K., Ackermann, M., et al. 2018b, Sci, 361, 147
Aartsen, M. G., Abraham, K., Ackermann, M., et al. 2018c, ApJ, 857, 117
Aartsen, M. G., Abraham, K., Ackermann, M., et al. 2020a, PhRvL, 125, 121104
Aartsen, M. G., Abraham, K., Ackermann, M., et al. 2020b, PhRvL, 124, 051103
Aartsen, M. G., Abraham, K., Ackermann, M., et al. 2020c, ApJ, 890, 111
Aartsen, M. G., Abraham, K., Ackermann, M., et al. 2020d, JCAP, 2020, 042
Aartsen, M. G., Abraham, K., Ackermann, M., et al. 2020e, ApJ, 898, 117
Aartsen, M. G., Abraham, K., Ackermann, M., et al. 2020f, ApJL, 898, L10
Aartsen, M. G., Abraham, K., Ackermann, M., et al. 2020g, ApJ, 892, 53
Aartsen, M. G., Ackermann, M., Adams, J., et al. 2014, PhRvL, 113, 101101
Aartsen, M. G., Ackermann, M., Adams, J., et al. 2017a, ApJ, 843, 112
Aartsen, M., et al. 2017, ApJ, 835, 45
Abbasi, R., Abdou, Y., Abu-Zayyad, T., et al. 2010, NIMPA, 618, 139
Abbasi, R., Abdou, Y., Abu-Zayyad, T., et al. 2012, A&A, 539, A60
Abbasi, R., Ackermann, M., Adams, J., et al. 2009, NIMPA, 601, 294
Abbott, B. P., Abbott, R., Abbott, T. D., et al. 2017, PhRvL, 119, 161101
Acciari, V., Ansoldi, S., Arbet Engels, A., et al. 2019a, Natur, 575, 455
Acciari, V., Ansoldi, S., Arbet Engels, A., et al. 2019b, Natur, 575, 459
Achterberg, A., Ackermann, M., Adams, J., et al. 2006, APh, 26, 155
Ackermann, M., et al. 2015, ApJ, 799, 86
Ahlers, M., & Halzen, F. 2018, PrPNP, 102, 73
Albert, A., André, M., Anghinolfi, M., et al. 2017, ApJL, 850, L35
Albert, A., André, M., Anghinolfi, M., et al. 2019, ApJ, 870, 134
Alexandreas, D., Berley, D., Biller, S., Dion, G., & Goodman, J. 1993, NIMPA, 328, 570
Angioni, R., Nesci, R., Finke, J. D., Buson, S., & Ciprini, S. 2019, A&A, 627, A140
ANTARES Collaboration, Albert, A., André, M., et al. 2020, EPJC, 80, 487
Arcavi, I., Wolf, W. M., Howell, D. A., et al. 2016, ApJ, 819, 35
Aublin, J., Illuminati, G., & Navas, S. 2019, arXiv:1908.08248

Barlow, R. 1990, NIMPA, 297, 496
Blaufuss, E., Kintscher, T., Lu, L., & Tung, C. F. 2020, PoS, ICRC2019, 1021
Bochenek, C. D., Ravi, V., Belov, K. V., et al. 2020, Natur, 587, 59
Braun, J., Baker, M., Dumm, J., et al. 2010, APh, 33, 175
Braun, J., Dumm, J., De Palma, F., et al. 2008, APh, 29, 299
Cassiday, G. L., Cooper, R., Dawson, B. R., et al. 1989, PhRvL, 62, 383
Cherenkov Telescope Array Consortium, Acharya, B. S., Agudo, I., et al. 2019, Science with the Cherenkov Telescope Array (Singapore: World Scientific)
Denton, P. B., & Tamborra, I. 2018, ApJ, 855, 37
Desiati, P., Kuwabara, T., Gaisser, T., Tilav, S., & Rocco, D. 2011, in 32nd Int. Cosmic Ray Conf., ICRC 2011 (New York: AIP), 78
Drout, M. R., Chornock, R., Soderberg, A. M., et al. 2014, ApJ, 794, 23
Evans, P. A., Osborne, J. P., Kennea, J. A., et al. 2015, MNRAS, 448, 2210
Fang, K., Banerjee, A., Charles, E., & Omori, Y. 2020, ApJ, 894, 112
Fang, K., Metzger, B. D., Murase, K., Bartos, I., & Kotera, K. 2019, ApJ, 878, 34
Goldstein, A., Veres, P., Burns, E., et al. 2017, ApJL, 848, L14
Gorski, K., Hivon, E., Banday, A., et al. 2005, ApJ, 622, 759
Grashorn, E., de Jong, J., Goodman, M., et al. 2010, APh, 33, 140
Gupta, P. D., & Saini, N. 2018, JApA, 39, 14
Haack, C., & Wiebusch, C. 2018, PoS, ICRC2017, 1005
Halzen, F., Kheirandish, A., Weisgarber, T., & Wakely, S. P. 2019, ApJL, 874, L9
Hunter, J. 2007, CSE, 9, 90
Hussain, R., Vandenbroucke, J., & Wood, J. 2020, PoS, ICRC2019, 918
Keivani, A., Veske, D., Countryman, S., et al. 2020, PoS, ICRC2019, 930
Kintscher, T. 2016, J. Phys. Conf. Ser., 718, 062029
Li, X., Zhou, B., He, H.-N., Fan, Y.-Z., & Wei, D.-M. 2014, ApJ, 797, 33
Lu, W., & Piro, A. L. 2019, ApJ, 883, 40
Margutti, R., Metzger, B. D., Chornock, R., et al. 2019, ApJ, 872, 18
McKinney, W. 2010, in Proc. 9th Python in Science Conf., ed. S. fan van der Walt & J. Millman, 56
Meagher, K. 2018, PoS, ICRC2017, 1007
Meagher, K., Pizzuto, A., & Vandenbroucke, J. 2020, PoS, ICRC2019, 1026
Metzger, B. D., Fang, K., & Margalit, B. 2020, ApJL, 902, L22
Molla, M. 2020, Neutrino2020 (Poster Session), 244, https://indico.fnal.gov/event/19348/contributions/186268/
Price-Whelan, A. M., Sipőcz, B. M., Günther, H. M., et al. 2018, AJ, 156, 123
Rest, A., Garnavich, P. M., Khatami, D., et al. 2018, NatAs, 2, 307
Savchenko, V., Ferrigno, C., Kuulkers, E., et al. 2017, ApJL, 848, L15
Schneider, A. 2020, PoS, ICRC2019, 1004
Schumacher, L. 2019, EPJ Web Conf., 207, 02010
Senno, N., Murase, K., & Mészáros, P. 2016, PhRvD, 93, 083003
Stein, R. 2020, PoS, ICRC2019, 1016
Stein, R., Necker, J., Bradascio, F., & Garrappa, S. 2020, IceCubeOpenSource/flarestack: Titan V2.2.3, v2.2.3, Zenodo, doi:10.5281/zenodo.4005800
Stettner, J. 2020, PoS, ICRC2019, 1017
Strotjohann, N. 2020, PhD Thesis, Deutsches Elektronen-Synchrotron
Tamborra, I., & Ando, S. 2016, PhRvD, 93, 053010
The CHIME/FRB Collaboration, Andersen, B. C., Bandura, K. M., et al. 2020, Natur, 587, 54
Tilav, S., Desiati, P., Kuwabara, T., et al. 2010, arXiv:1001.0776
Van der Walt, S., Colbert, S. C., & Varoquaux, G. 2011, CSE, 13, 22
Virtanen, P., Gommers, R., Oliphant, T. E., et al. 2020, Nat. Method, 17, 261
Waxman, E., & Bahcall, J. 1997, PhRvL, 78, 2292